Dynamic analysis and response attenuation of a two-degree-of-freedom structure with a variable inertia rotational mechanism subjected to ground excitation

Anika T. Sarkar[a], and Nicholas E. Wierschem[a*]

[a] Department of Civil and Environmental Engineering, The University of Tennessee
325 John D. Tickle Engineering Building, 851 Neyland Drive, Knoxville TN 37996-2313

*Corresponding author: nwiersch@utk.edu

Abstract

Rotational inertia mechanisms offer innovative possibilities for mitigating the effects of dynamic loads on structures. While conventional approaches to structural response modification involve modifying stiffness, strength and damping, a promising alternative lies in the variable inertia rotational mechanism (VIRM), which represents a novel approach for variably shifting the effective mass of a structure. Despite its potential, the vibration mitigation effectiveness of the VIRM under seismic loads and its influence on frequency shifts with complex loading environments remain a gap in current understanding. This study explores the impact of the VIRM on a two-degree-of-freedom (2DOF) structure subjected to white noise loading and seismic ground motions. Through a numerical assessment of this structure with single and multiple VIRMs and considering different inertance ratios and load amplitudes, this study seeks to investigate the frequency shifts and the efficacy of VIRM in reducing structural response. The findings of this study highlight the potential of VIRM's to alter natural frequencies and mitigate structural response under different load scenarios. This study addresses existing gaps in knowledge and contributes valuable insights into the interplay of VIRM parameters, frequency shifts, and the effectiveness of VIRMs for enhancing structural performance and seismic protection.

Keywords: Variable inertia, Instantaneous frequency, Incremental dynamic analysis, Seismic, Passive control

1 Introduction

Civil engineering structures can experience adverse effects when subjected to dynamic loads such as seismic excitation and wind. The behavior and response of a structure can be modified by altering the stiffness, strength, and damping of that structure [1], [2], [3], [4], [5]. However, alternative passive control devices utilizing supplemental rotational inertia mechanisms (RIMs) have been developed to modify the effective mass of a structure [6], [7], [8], [9], [10]. Arakaki et al. first proposed using a rotary damper in the late 1990s, which combines a ball screw assembly and cylindrical mass rotating inside a chamber filled with a viscous fluid, to modify the seismic response of structures [6], [11]. These supplemental rotational inertia devices transform the relative displacement between the terminals to rotational motion of a flywheel. In the force-current analogy, these devices function as a mechanical counterpart of an electrical capacitor. This analogical relationship was initially identified by Smith, who introduced the term 'inerter' in 2002 for any mechanical arrangement where the resultant force is proportional to the relative acceleration between its two terminals [7].

Inerters can be physically realized with mechanical mechanisms such as a ball-screw or rack and pinion assembly with a flywheel, or with fluid-based or electromagnetic-based mechanisms [7], [12], [13], [14], [15]. The output force of an inerter is proportional to the relative acceleration between its terminals. The constant of proportionality is called inertance and has the same units as mass. One of the distinguishing features of the inerter is its mass amplification effect. Due to this mass amplification effect, the inerter can produce substantial inertial mass with minimal physical mass.

Upon its conceptual development and initial experimental validation, the inerter has been studied in vehicle mechanics and dynamics to control suspension vibration [16], [17] and has also

been proposed for wind and seismic protection of civil structures. In civil structures, these mechanisms are often combined with other control applications, such as tuned mass dampers, viscous dampers, toggle braces, external rocking walls, negative stiffness devices, and friction pendulums, to enhance performance [18], [19], [20], [21], [22], [23], [24]. These systems are examined in applications, such as optimal design and seismic protection of building structures [25], [26], improving base isolation systems [8], [27], and mitigating wind-induced vibration of tall buildings [18], [28] and cable-stayed bridges [23], [24]. Researchers have also investigated inerter-based devices in multi-degree-of-freedom (MDOF) structures to examine the natural frequency changes [29] and enhance performance of tuned damper systems [25], [30], [31]. Furthermore, inerter-based dampers, such as multi-tuned damper inerter [32] and multi-tuned liquid column damper inerter [33], have been investigated to control the seismic vibration of adjacent high-rise buildings.

While inerters are characterized by linear behavior and constant resulting inertance, another branch of research explores nonlinear mechanisms with variable inertance [34], [35], [36], [37], [38]. Variable inertance can be produced in multiple ways including exploiting geometrically nonlinear configurations of otherwise linear inerters [34], [39] or by modifying the rotational inertia of the mechanism's flywheel [37], [38], [40], [41], [42], [43], [44]. This study considers one such mechanism, called the variable inertia rotational mechanism (VIRM), which employs a flywheel that contains masses that can move within the flywheel and thus produce variations in the flywheel's rotational inertia [37], [38], [40], [41], [42]. This variable rotational inertia can cause notable modifications to the dynamics of the host structure, thereby VIRMs offer a potential for integration into vibration control strategies.

In vehicle systems research, VIRMs have demonstrated improvements in rider comfort, better road handling and safety, and decreased suspension deflection under most circumstances [40], [41]. VIRMs have also been studied to increase power absorption bandwidth, increase vibration mitigation, and enhance stability in power systems, such as hydraulic motors, diesel generators, wave energy converters, and wind turbine rotors [37], [42], [43], [44], [45]. However, many of these studies have considered active and semi-active versions of the VIRM, not the passive VIRM [44], [45], [46].

While applications in other fields have been considered in different research studies, the investigation of the potential of VIRMs in civil engineering structures is less developed. Furthermore, the authors are unaware of any VIRM implemented in civil engineering structures. The existing research has yet to investigate the impact of VIRMs under seismic ground motion or random noise. While limited studies on VIRM indicate effectiveness in reducing the response amplitude of dynamic systems, their influence on instantaneous frequency has not been fully studied. Additionally, the effect of VIRMs on MDOF system dynamics remains unexplored. As a result, there is a notable gap in understanding the impact of variable rotational inertia on the frequency shifts and response of MDOF systems subjected to seismic ground motion and random noise.

The novelty of this study is that it aims to address these gaps in knowledge and numerically evaluate the frequency shifts and effectiveness of VIRM in reducing the response of a two-degree-of-freedom (2DOF) structure. This investigation includes scenarios with a structure with single and multiple passive VIRMs that is subjected to seismic ground motion and white noise loading. The study also explores the effect of VIRM inertance ratios and changes in load amplitude on the frequency shifts and response reduction. The computed response quantities for the 2DOF structure

with VIRMs will be compared to those of a structure with fixed inertia rotational mechanisms (FIRMs).

This paper is structured as follows. In Section 2, the mechanics of the VIRM and mathematical models of a 2DOF structure with one or two VIRMs are described. Section 3 introduces the parameters of the structure and the loading considered in this study as well as the response measures that will be used to evaluate the effect of the VIRM. The impact of VIRM on natural frequency shifts is presented in Section 4, while Section 5 discusses the impact of the VIRM on an H_2 response measure. Section 6 presents results from incremental dynamic analyses investigating the effects of VIRM on the response of the structures to various ground motions. The impact of the inertance ratio and loading amplitude are also considered in the results presented in Sections 4, 5 and 6. Finally, the study is summarized and conclusions are presented in Section 7.

2 Equations of motion of 2DOF structure with variable inertia rotational mechanism

Figure 1(a) depicts the 2DOF primary structure that is considered in this numerical study, which has two identical VIRMs attached between the ground and the first floor and between the first and the second floors. In Figure 1(b), the two DOF primary structure has one VIRM that is attached between the ground and the first floor of the structure. In both Figure 1(a) and Figure 1(b), the first and second story masses are m_{s_1} and m_{s_2}, and k_{s_1}, k_{s_2}, c_{s_1} and c_{s_2} are the stiffness and the viscous damping coefficients of the two stories. In this study, two other RIM configurations are investigated in the 2DOF primary structure: one where the two VIRMs are replaced with two identical fixed inertia rotational mechanisms (FIRMs) and another where the single VIRM is replaced with a single FIRM. In comparison to a VIRM, all components of a FIRM maintain a fixed configuration irrespective of the flywheel's rotational velocity.

The VIRM considered in this study is shown in Figure 2 and utilizes a ball screw mechanism to transfer the relative translational motion of a story of the structure in to rotational motion of the device's flywheel. In this study, the VIRM features a flywheel hub with four symmetrically spaced guide tracks and four discrete masses on the guide tracks that are connected to the flywheel hub with trilinear stiffness elements, as illustrated in Figure 2. It is assumed that the slider masses in each flywheel are synchronously moving with the same radial motion. The motion of the VIRM slider masses are damped with each slider mass modeled as connected to a viscous damper with coefficient c_{sd}; however, as in the example physical realization shown in Figure 2a, this slider damping may result from inherent damping in the slider instead of a discrete viscous damping source. When the flywheel is at rest, the masses are located at an initial radial position, x_0, near the center of the flywheel. As the flywheel rotational velocity increases, centrifugal force drives the masses to move radially outward, while the springs attached to the flywheel masses make the masses slide back toward their original position given decreases in the rotational velocity. The radial movement of the masses causes a restoring force in the springs that increases with the change in the radial position of the masses.

The mathematical model of the springs assumes a trilinear elastic force-displacement relationship that has a relatively low stiffness at the center (k_{sd}) between two relatively stiff penalty spring segments (k_p), as illustrated in Figure 2(c). When the flywheel masses approach the upper bound contact point (R_{ubc}) near the end nut or the lower bound contact point (R_{lbc}) near the flywheel hub, as shown on Figure 2, the penalty spring stiffness segments work to further restrain the movement of the slider masses. This behavior mimics the behavior of springs that would stiffen as they approach being fully compressed.

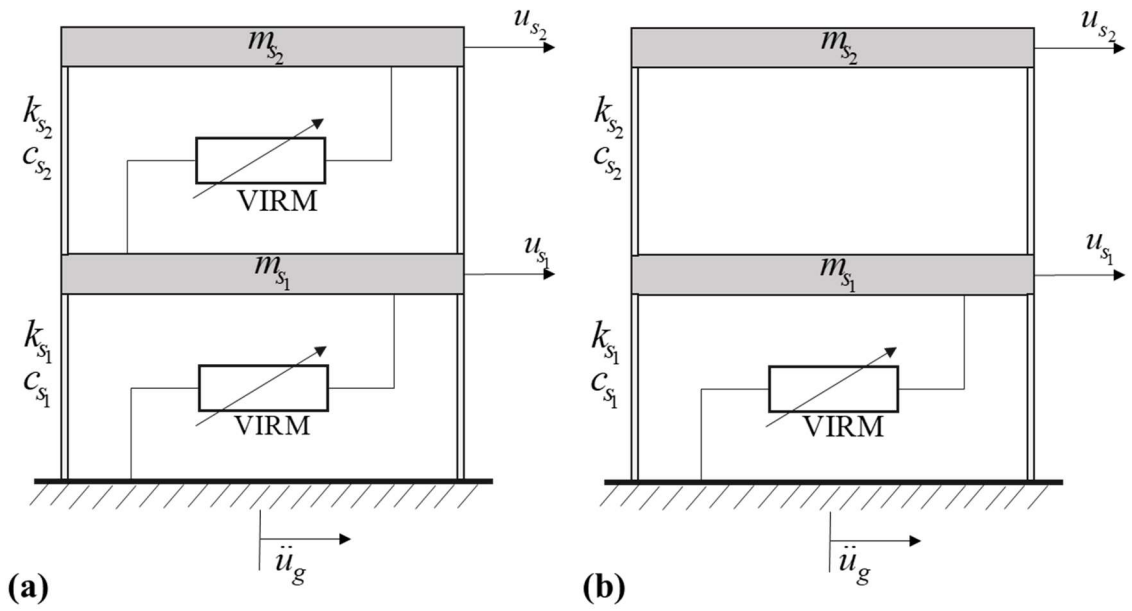

Figure 1. (a) 2DOF primary structure with two VIRMs (2VIRM structure) (b) 2DOF primary structure with one VIRM (1VIRM structure)

The rotational velocity of the flywheel of the VIRM is proportional to the relative velocity between the two attachment points on the structure. The relationship can be expressed as

$$\begin{aligned} \dot{\theta}_1 &= \alpha_1 \left(\dot{u}_{s_1} - \dot{u}_g \right) \\ \dot{\theta}_2 &= \alpha_2 \left(\dot{u}_{s_2} - \dot{u}_{s_1} \right) \end{aligned} \tag{1}$$

where $\dot{\theta}_1$ and $\dot{\theta}_2$ are the rotational velocities of the two VIRM flywheels, and $\dot{u}_{s_1}, \dot{u}_{s_2}$, and $\dot{u}_g$ are the absolute velocities of m_{s_1}, m_{s_2} and the ground. α_1 and α_2 are the proportionality coefficients governing this relationship. In this study, $\alpha_1 = \alpha_2 = \alpha$ and $\alpha = \frac{2\pi}{\rho}$ for a ball-screw mechanism where ρ is the lead of the ball-screw.

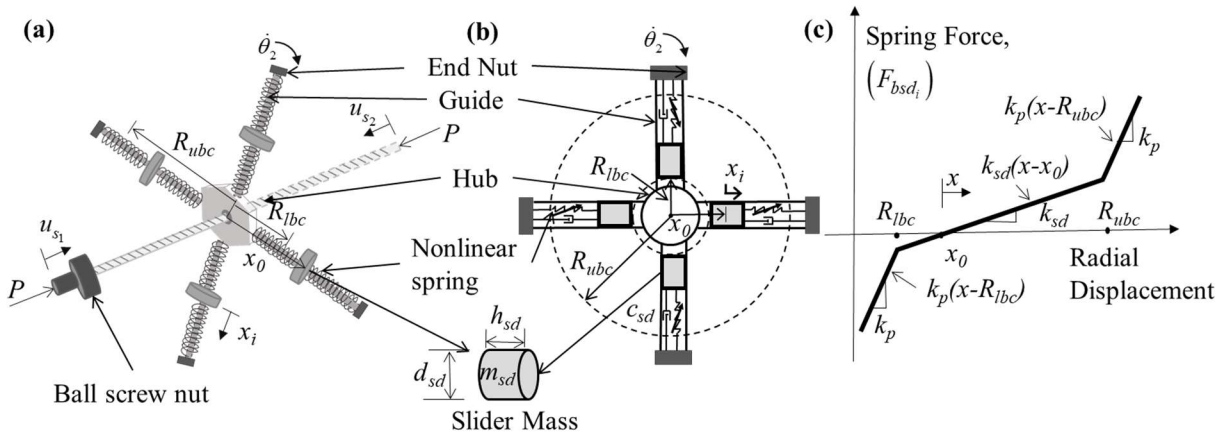

Figure 2. (a) Potential realization of VIRM, (b) Schematic diagram of the VIRM flywheel, (c) Trilinear force displacement relationship for the spring connected to the slider mass

The equations defining the restoring force of the trilinear spring ($F_{bsd_i}(x_i)$) as a function of the radial displacement of the slider masses of the VIRM in the ith story (x_i) are

$$\begin{aligned} F_{bsd_i}(x_i) &= k_{sd}(R_{lbc} - x_0) + k_p(x_i - R_{lbc}),\ x_i < R_{lbc} \\ F_{bsd_i}(x_i) &= k_{sd}(x_i - x_0),\ R_{lbc} \le x_i < R_{ubc} \\ F_{bsd_i}(x_i) &= k_{sd}(R_{ubc} - x_0) + k_p(x_i - R_{ubc}),\ x_i \ge R_{ubc} \end{aligned} \tag{2}$$

The moment of inertia of the flywheel of the VIRM can be divided into constant and variable parts. The constant portion of the VIRM moment of inertia is

$$J_{\text{constant}} = \left(\frac{1}{12} n_i m_{sd}\left(\frac{3}{4} {d_{sd}}^2 + {h_{sd}}^2\right) + \frac{1}{2} m_c r^2\right) \tag{3}$$

where n_i, m_{sd}, d_{sd}, h_{sd}, m_c and r are the number of sliders in the VIRM in the ith story, slider masses, slider diameter, slider height, mass of the flywheel without the sliders, and radius of the flywheel, respectively. The variable part of the moment of inertia is related to the radial position of the slider masses; when the slider masses move along the guided slot of the VIRM flywheel, the moment of inertia changes. The mass effects provided by the VIRM to the structure increase as the moment

of inertia of the VIRM increases. Besides the ability of the slider masses to move during the response of the structure, the VIRM and FIRM flywheels have the same physical properties. The moment of inertia of the flywheel of the VIRM and FIRM flywheels in the ith story can be expressed as

$$\begin{aligned} J_{VIRM_i} &= J_{\text{constant}} + n_i m_{sd} x_i^2 \\ J_{FIRM_i} &= J_{\text{constant}} + n_i m_{sd} y^2 \end{aligned} \tag{4}$$

The fixed position of the slider mass of the FIRM is denoted by y in Equation (4). In this study, y is set as either $x_{0,}$ the initial position of the masses in the VIRM, or R_{ubc}, the upper bound contact point.

The equations of motion of the 2DOF primary structure with two VIRM, which is shown in Figure 1(a) and hereafter referred to as the 2VIRM structure, can be derived using the Lagrangian method. The detailed derivation is presented in the Appendix. For this derivation, it is assumed that the two VIRMs have identical properties. The Lagranges' equation of motion in generalized coordinates can be defined as

$$\frac{d}{dt}\frac{\partial \mathrm{T}}{\partial \dot{q}_i} - \frac{\partial \mathrm{T}}{\partial q_i} + \frac{\partial V}{\partial q_i} = p_i(t),\ i = 1,2,3,4; \tag{5}$$

where q_1, q_2, q_3, q_4 are the displacements relative to the ground of the two masses of the primary structure (u_{s_1} and u_{s_2}) and the radial displacements of the slider masses in the two VIRMs (x_1 and x_2); T and V denote the kinetic energy and potential energy of the dynamic system, respectively.

The kinetic energy of the system can be formulated from the motion of the masses of the structure's floors, rotation of the flywheels, and radial and tangential velocity of the slider masses in the flywheels. The potential energy includes the elastic energy stored in all the springs, including

elastic energy stored in the springs related to the structural stiffness (k_{s_1}, k_{s_2}) and the VIRM stiffness (k_{sd}, k_p). The gravitational effect on the slider mass movement is not considered here. The non-conservative forces include the externally applied forces as well as the damping forces associated with the VIRM slider masses and the inherent damping of the structure.

The equations of motion of the 2VIRM structure subjected to an absolute ground acceleration are

$$
\begin{aligned}
&m_{s_1}\ddot{u}_{s_1} + J_{VIRM_1}\alpha^2\left(\ddot{u}_{s_1} - \ddot{u}_g\right) - J_{VIRM_2}\alpha^2\left(\ddot{u}_{s_2} - \ddot{u}_{s_1}\right) + \left(2n_1 m_{sd} x_1 \alpha^2 \dot{u}_{s_1}\right)\dot{x}_1 - \left(2n_2 m_{sd} x_2 \alpha^2\left(\dot{u}_{s_2} - \dot{u}_{s_1}\right)\right)\dot{x}_2 \\
&+\left(c_{s_2} + c_{s_1}\right)\dot{u}_{s_1} - c_{s_2}\dot{u}_{s_2} - c_{s_1}\dot{u}_g + \left(k_{s_1} + k_{s_2}\right)u_{s_1} - k_{s_2}u_{s_2} - k_{s_1}u_g = -m_{s_1}\ddot{u}_g \\
&m_{s_2}\ddot{u}_{s_2} + J_{VIRM_2}\alpha^2\left(\ddot{u}_{s_2} - \ddot{u}_{s_1}\right) + 2n_2 m_{sd} x_2 \alpha^2\left(\dot{u}_{s_2} - \dot{u}_{s_1}\right)\dot{x}_2 + k_{s_2}\left(u_{s_2} - u_{s_1}\right) - c_{s_2}\dot{u}_{s_1} + c_{s_2}\dot{u}_{s_2} = -m_{s_2}\ddot{u}_g \\
&m_{sd}\ddot{x}_1 - m_{sd} x_1 \alpha^2\left(\dot{u}_{s_1} - \dot{u}_g\right)^2 + F_{bsd_1}\left(x_1\right) + c_{sd}\dot{x}_1 = 0 \\
&m_{sd}\ddot{x}_2 - m_{sd} x_2 \alpha^2\left(\dot{u}_{s_2} - \dot{u}_{s_1}\right)^2 + F_{bsd_2}\left(x_2\right) + c_{sd}\dot{x}_2 = 0
\end{aligned}
\tag{6}
$$

The equations of motion for the primary structure with 1 VIRM in its first story, which is shown in Figure 1(c) and hereafter referred to as the 1VIRM structure, are shown in Equation (7). Note that the $F_{bsd_1}\left(x_1\right)$ in Equation (6) and Equation (7), and $F_{bsd_2}\left(x_2\right)$ in Equation (6) are the expressions of the nonlinear spring restoring force of the VIRM's attached at the 1st and 2nd story, respectively, as established in Equation (2).

$$
\begin{aligned}
&m_{s_1}\ddot{u}_{s_1} + J_{VIRM_1}\alpha^2\left(\ddot{u}_{s_1} - \ddot{u}_g\right) + \left(2nm_{sd} x_1 \alpha^2 \dot{u}_{s_1}\right)\dot{x}_1 + \left(c_{s_2} + c_{s_1}\right)\dot{u}_{s_1} - c_{s_2}\dot{u}_{s_2} + \left(k_{s_1} + k_{s_2}\right)u_{s_1} - k_{s_2}u_{s_2} = -m_{s_1}\ddot{u}_g \\
&m_{s_2}\ddot{u}_{s_2} + k_{s_2}\left(u_{s_2} - u_{s_1}\right) + c_{s_2}\left(\dot{u}_{s_2} - \dot{u}_{s_1}\right) = -m_{s_2}\ddot{u}_g \\
&m_{sd}\ddot{x}_1 - m_{sd} x_1 \alpha^2 \dot{u}_{s_1}{}^2 + F_{bsd_1}\left(x_1\right) + c_{sd}\dot{x}_1 = 0
\end{aligned}
\tag{7}
$$

In order to evaluate the impact of the VIRM, comparisons will be made to cases where the VIRMs are replaced with FIRMs. The system where identical FIRMs are placed in each story of the primary structure is referred to as the 2FIRM structure and the system where a FIRM is

positioned in just the 1st story is referred to as the 1FIRM structure. The equations of motion for the 2FIRM structure and 1FIRM structure are shown in Equation (8) and Equation (9), respectively. Note that the systems in Equation (8) and Equation (9) are the natural result of the systems in Equations (6) and Equation (7) with the slider masses fixed at radial position *y*.

$$\begin{aligned} &m_{s_1}\ddot{u}_{s_1} + J_{FIRM_1}\alpha^2\left(\ddot{u}_{s_1} - \ddot{u}_g\right) - J_{FIRM_2}\alpha^2\left(\ddot{u}_{s_2} - \ddot{u}_{s_1}\right) + \left(c_{s_2} + c_{s_1}\right)\dot{u}_{s_1} - c_{s_2}\dot{u}_{s_2} - c_{s_1}\dot{u}_g \\ &+\left(k_{s_1} + k_{s_2}\right)u_{s_1} - k_{s_2}u_{s_2} = -m_{s_1}\ddot{u}_g \\ &m_{s_2}\ddot{u}_{s_2} + J_{FIRM_2}\alpha^2\left(\ddot{u}_{s_2} - \ddot{u}_{s_1}\right) + k_{s_2}\left(u_{s_2} - u_{s_1}\right) - c_{s_2}\dot{u}_{s_1} + c_{s_2}\dot{u}_{s_2} = -m_{s_2}\ddot{u}_g \end{aligned} \tag{8}$$

$$\begin{aligned} &m_{s_1}\ddot{u}_{s_1} + J_{FIRM_1}\alpha^2\ddot{u}_{s_1} + \left(c_{s_2}+c_{s_1}\right)\dot{u}_{s_1} - c_{s_2}\dot{u}_{s_2} + \left(k_{s_1}+k_{s_2}\right)u_{s_1} - k_{s_2}u_{s_2} = -m_{s_1}\ddot{u}_g \\ &m_{s_2}\ddot{u}_{s_2} + k_{s_2}\left(u_{s_2}-u_{s_1}\right) + c_{s_2}\left(\dot{u}_{s_2}-\dot{u}_{s_1}\right) = -m_{s_2}\ddot{u}_g \end{aligned} \tag{9}$$

Additional comparisons will be made with the primary structure without a VIRM or FIRM. This structure will be referred to as the no control structure and the equations of motion are similar to the structures with FIRM, excluding the moment of inertia terms. For convenience, the following ratios are defined and will be utilized throughout this paper. $\mu_{flywheel} = \left(n * m_{sd} + m_c\right)/m_{s_i}$:flywheel mass ratio; ω_{s_i}: ith mode natural frequency of the primary structure without VIRM/FIRM; $\xi_s = c_s / 2m_s\omega_{s_i}$: primary structure damping ratio;

3 System parameters and response measures

This section presents the parameters of the systems and the loading parameters utilized in the analysis of these systems. The range of possible mass effects that are produced by the VIRM given these parameters is also presented. Furthermore, the response measures used in the subsequent section to evaluate system dynamics and performance are introduced.

3.1 System and analysis parameters

The results of numerical simulations will be used to compare the dynamic behavior and response of the systems described in the previous section (Equations (6)-(9)). These numerical simulations are performed using the MATLAB implicit solver [47] with an output frequency set at 4000 Hz. The structure is excited using a band-limited white noise (BLWN) ground acceleration with a frequency range of 1 to 15 Hz, as well as seismic loading. The broadband excitation provided by the BLWN is well-suited for investigating the resulting changes in the structure's dynamic properties. Using the 50 seismic records of the FEMA P695 far-field and near-field earthquake sets [48], differences in the seismic response of the structural configurations are assessed with a specific focus on median maximum story drift and acceleration.

The system parameters selected for this study are shown in Table 1. The resulting natural frequencies of the structure and linearized natural frequencies of the slider mass are between 1-10 Hz. The structural damping coefficients were selected so that the 2DOF structure itself has 2% inherent damping in each mode and the resulting physical damping coefficients were utilized for the other structural configurations.

Table 1. System parameter values

Symbol	Description	Value
$m_{s_1} = m_{s_2}$	First and second story mass	300 kg
$k_{s_1} = k_{s_2}$	First and second story stiffness	320000 N/m
$\omega_1(no\,control)$	1st mode natural frequency (no control)	3.21 Hz
$\omega_2(no\,control)$	2nd mode natural frequency (no control)	8.41 Hz
ξ_s	Damping ratio in each mode of the primary system without VIRM/FIRM	2%
$\mu_{flywheel}$	Flywheel mass ratio	0.003, 0.008, 0.015
m_c	Flywheel mass (without sliders)	0.5 kg

$n_1 = n_2$	Number of sliders in the VIRM in the 1st and 2nd story	4
c_{sd}	Slider damping coefficient	5 Ns/m
k_{sd}	Slider soft stiffness	30 N/m
k_p	Slider penalty stiffness	6000 N/m
d_{sd}	Slider diameter	0.02 m
h_{sd}	Slider height	0.015 m
R	Flywheel radius	0.1 m
x_0	Initial position	0.02 m
R_{ubc}	Radial position of the upper penalty spring	0.095 m
R_{lbc}	Radial position of the lower penalty spring	0.005 m
α	Proportionality constant between relative structure velocity and flywheel angular velocity	200 (rad/m)

Depending on the radial position of the slider masses in the flywheel, the moment of inertia of the flywheels of the VIRM change, as well as the mass effects they provide. The inertance $\left(b_{2VIRM_1}, b_{2VIRM_2}, b_{1VIRM_1}\right)$ and inertance ratios $\left(\beta_{2VIRM_1}, \beta_{2VIRM_2}, \beta_{1VIRM}\right)$ are defined as,

$$
\begin{aligned}
&b_{2VIRM_1} = J_{VIRM,1}\alpha^2 + J_{VIRM,2}\alpha^2;\ b_{2VIRM_2} = J_{VIRM,2}\alpha^2;\ b_{1VIRM} = J_{VIRM,1}\alpha^2 \\
&\beta_{2VIRM_1} = \frac{b_{2VIRM_1}}{m_{s_1} + m_{s_2}};\ \beta_{2VIRM_2} = \frac{b_{2VIRM_2}}{m_{s_1} + m_{s_2}};\ \beta_{1VIRM} = \frac{b_{1VIRM}}{m_{s_1} + m_{s_2}};
\end{aligned} \tag{10}
$$

Figure 3 presents the effect of flywheel mass changes and the changes in slider mass position on the inertance ratios of the VIRM in the 2VIRM and 1VIRM structures. The figure shows that the inertance ratio increases as the sliders move out radially. This increase in inertance ratios with respect to slider position is consistent across all flywheel mass ratios considered for the 2VIRM and 1VIRM structures. Additionally, the inertance ratio of the 2VIRM structure is comparatively higher than the 1VIRM structure, particularly at higher flywheel mass ratios and

greater slider displacement. For instance, at flywheel mass ratio of 0.015, the maximum inertance ratio of the 2VIRM structure is 5.5, compared to 3 for the 1VIRM structure.

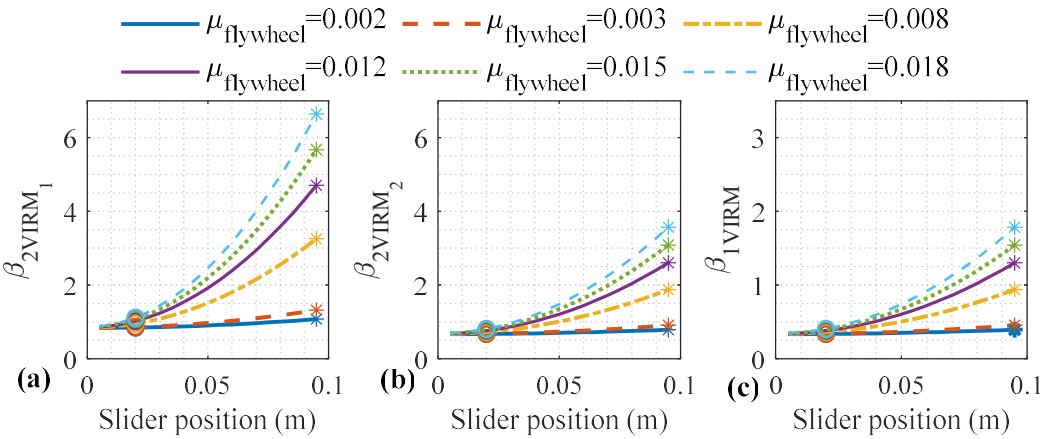

Figure 3. Inertance ratios across different flywheel mass ratios and a range of slider mass radial positions (a) β_{2VIRM_1}, (b) β_{2VIRM_2} and (c) β_{1VIRM}. Note that marker legends are Blue: $\mu_{flywheel} = 0.002$ Orange: $\mu_{flywheel} = 0.003$, Yellow: $\mu_{flywheel} = 0.008$, Purple: $\mu_{flywheel} = 0.012$, Green: $\mu_{flywheel} = 0.015$, and Sky blue: $\mu_{flywheel} = 0.018$, '*' denotes FIRM (at R_{ubc}), 'o' denotes FIRM (at x_0)

3.2 Response Measures

As described in the following sub-sections, various response measures are computed to assess the dynamic behavior and response in this study. The shifts in the natural frequencies are evaluated using wavelet transforms. Other natural frequency measures considered include instantaneous frequency (ω_{IF}) and weighted average instantaneous frequency. Peak time-history responses and an estimated H_2 norm analog $(\tilde{H}_2)$ are used to investigate structural performance changes with the VIRM. The natural frequency measures and the estimated H_2 norm analog are evaluated considering BLWN loading, while median peak responses from seismic ground motions are determined from a study utilizing incremental dynamic analysis.

3.2.1 Natural Frequency Measures

3.2.1.1 Wavelet Transform

The wavelet transform is a tool that can be used to assess vibrational energy distribution in the time and frequency domains. The Morlet wavelet is adopted as the mother wavelet for its simplistic time-domain and frequency-domain analytical forms. As wavelet transforms capture the temporal variability of frequency content, this tool can be effective in examining how the nonlinearity of the VIRM impacts the structure's effective natural frequency over the duration of the analysis time considered.

3.2.1.2 Instantaneous Frequency

The ω_{IF} represents the preferred vibration frequency of a dynamic system. In a linear system, the ω_{IF} remains constant and matches the system's natural frequency. However, for nonlinear systems, the ω_{IF} continuously changes with the response of the system. In this study, the ω_{IF} is estimated by an eigenvalue analysis of the tangent mass and tangent stiffness matrices at each time step during the response of the system. These matrices for a n-DOF system can be evaluated using Equation (11), where $\mathbf{F_{int}}$ contains the internal forces of the nonlinear structure, which is a function of the system DOF (u) and the derivatives of the DOFs $(\dot{u},\ddot{u})$.

$$\mathbf{K_t}\left(\mathbf{u},\dot{\mathbf{u}},\ddot{\mathbf{u}}\right)=\frac{\partial \mathbf{F_{int}}}{\partial \mathbf{u}}=\begin{bmatrix} \frac{\partial \mathbf{F}_{\mathbf{int},1}}{\partial \mathbf{u}_1} & \frac{\partial \mathbf{F}_{\mathbf{int},1}}{\partial \mathbf{u}_2} & .... & \frac{\partial \mathbf{F}_{\mathbf{int},1}}{\partial \mathbf{u}_n} \\ \frac{\partial \mathbf{F}_{\mathbf{int},2}}{\partial \mathbf{u}_1} & \frac{\partial \mathbf{F}_{\mathbf{int},2}}{\partial \mathbf{u}_2} & .... & \frac{\partial \mathbf{F}_{\mathbf{int},2}}{\partial \mathbf{u}_n} \\ . & . & . & . \\ . & . & . & . \\ \frac{\partial \mathbf{F}_{\mathbf{int},n}}{\partial \mathbf{u}_1} & \frac{\partial \mathbf{F}_{\mathbf{int},n}}{\partial \mathbf{u}_2} & .... & \frac{\partial \mathbf{F}_{\mathbf{int},n}}{\partial \mathbf{u}_n} \end{bmatrix};\mathbf{M_t}\left(\mathbf{u},\dot{\mathbf{u}},\ddot{\mathbf{u}}\right)=\frac{\partial \mathbf{F_{int}}}{\partial \ddot{\mathbf{u}}}=\begin{bmatrix} \frac{\partial \mathbf{F}_{\mathbf{int},1}}{\partial \ddot{\mathbf{u}}_1} & \frac{\partial \mathbf{F}_{\mathbf{int},1}}{\partial \ddot{\mathbf{u}}_2} & .... & \frac{\partial \mathbf{F}_{\mathbf{int},1}}{\partial \ddot{\mathbf{u}}_n} \\ \frac{\partial \mathbf{F}_{\mathbf{int},2}}{\partial \ddot{\mathbf{u}}_1} & \frac{\partial \mathbf{F}_{\mathbf{int},2}}{\partial \ddot{\mathbf{u}}_2} & .... & \frac{\partial \mathbf{F}_{\mathbf{int},2}}{\partial \ddot{\mathbf{u}}_n} \\ . & . & . & . \\ . & . & . & . \\ \frac{\partial \mathbf{F}_{\mathbf{int},n}}{\partial \ddot{\mathbf{u}}_1} & \frac{\partial \mathbf{F}_{\mathbf{int},n}}{\partial \ddot{\mathbf{u}}_2} & .... & \frac{\partial \mathbf{F}_{\mathbf{int},n}}{\partial \ddot{\mathbf{u}}_n} \end{bmatrix} \quad (11)$$

Unlike the addition of the FIRM, the addition of the VIRM adds an additional degree-of-freedom. Hence, the eigenvalue analysis yields three ω_{IF} for the 1VIRM structure and four ω_{IF} for the 2VIRM structure at each time step. The ω_{IF} presented in this study at each time step are the two ω_{IF} that have the most significant engagement of the primary structure, as judged by evaluating their mode shapes, and thus provide information most relevant to the behavior of the primary structure. The resulting two eigen frequencies are then sorted in descending order and are denoted by ω_{IF_1} and ω_{IF_2}, respectively.

3.2.1.3 Weighted Average Instantaneous Frequency

As the ω_{IF} changes over time, the weighted average instantaneous frequency, ϖ_w, is derived in order to present information on the overall frequency behavior of the structure. The ϖ_w is determined by averaging the time-history of the ω_{IF}, utilizing a weight factor corresponding to the structure's total energy time-history response, as defined in Equation (12). This averaging is performed on both ω_{IF_1} and ω_{IF_2}, with results for the two instantaneous frequencies denoted by ϖ_{w_1} and ϖ_{w_2}, respectively. The ϖ_w can then be normalized using the natural frequencies (ω_1, ω_2) of the no-control structure,

$$\varpi_w = \frac{\sum_{i=1}^{n} W_i \omega_i}{\sum_{i=1}^{n} W_i}; \quad \Psi_{\varpi_{w1}} = \frac{\varpi_{w_1}}{\omega_1}, \Psi_{\varpi_{w2}} = \frac{\varpi_{w_2}}{\omega_2} \tag{12}$$

where W_i and ω_i are the total energy and ω_{IF} of the structure at time step, respectively, and n is the total number of time steps in the response considered.

3.2.2 Performance Measures

3.2.2.1 H_2 norm analog

The H_2 norm quantifies system variance amplification; thus, in theory, could be used to assess the impact of the VIRM on the response of the primary structure under dynamic loading. Typically, the H_2 norm is analytically determined for a linear time invariant system using a frequency response function; however, this method is not possible for a structure with a VIRM as it is nonlinear. Alternatively, this study uses a response measure known as the H_2 norm analog, which will be denoted by $\tilde{H}_2$. The $\tilde{H}_2$ is determined by taking the square of the area under the estimated frequency response function of the structure's interstory displacement response due to the ground acceleration over a bounded frequency range of 1-15 Hz, which aligns with the frequency range of the band-pass filtered white noise loading used. The $\tilde{H}_2$ of each configuration considered is normalized by the $\tilde{H}_2$ of the no-control structure, expressed as

$$\Sigma = \frac{\tilde{H}_2\left(RIM\ configuration\right)}{\tilde{H}_2\left(no\ control\right)} \tag{13}$$

3.2.2.2 Incremental Dynamic Analysis Curves

Incremental dynamic analysis (IDA) is performed to quantify the impact of the VIRM on structural performance considering seismic loads. This analysis involves performing multiple nonlinear dynamic analyses of a structural model subjected to a suite of ground motions, with each ground motion scaled to several intensity measures. This process generates IDA curves that represent key measures of the resulting structural response parameterized against the intensity measures for each ground motion. In this study, the maximum absolute interstory displacement and maximum absolute story acceleration are chosen as the key structural response measures.

The IDA is performed using a set of 50 ground motions, sourced from the FEMA P695 dataset, encompassing both far-field and near-field earthquakes [48]. The near-field earthquake records consist of ground motions with and without pulse, with a total of 14 instances each. The ground motions are scaled in two steps, as outlined in Equation (14) and (15). Initially, a normalization factor obtained from FEMA P695 [48] is used to adjust the peak ground velocity of each ground motion to align with the median of the set. Subsequently, a scaling factor is employed to tailor the normalized ground motion to the targeted intensity measure for the specific analyses.

$$\ddot{x}_{g,applied} = normalization\ factor * scaling\ factor * \ddot{x}_{g,recorded} \tag{14}$$

The IDA curves generated in this study use the spectral intensity, S_T, as the intensity measure. In the expression for S_T in Equation (15), S_{NRT} represents the median 5% damped spectral acceleration of the normalized record set at the first mode period of the uncontrolled structure.

$$S_T = S_{NRT} * scaling\ factor \tag{15}$$

Obtained through linear interpolation of values from FEMA P695 using the uncontrolled structure's first mode period (0.2784 s) [48], the precise S_{NRT} values for near-field and far-field earthquakes are 0.9837 g and 0.7767 g, respectively.

Typically, the IDA is performed until a particular limit state, such as collapse or yield, of a structure is reached. As the structure models employed in this study are simplified and do not account for material nonlinearity and collapse, the analysis is performed up to a predetermined spectral intensity of 2g, rather than a selected limit state.

To capture and compare the overall trends derived from the results of the IDA, the responses of the RIM configurations are normalized against the no control case and the median

responses are computed by aggregating the results from seismic records at each intensity level for each configuration. Furthermore, the median absolute deviation is computed as a measure analogous to standard deviation but employing medians.

4 Frequency Shifts

In this section, instantaneous frequency (ω_{IF}), weighted average instantaneous frequency $(\omega_{\bar{w}})$, and wavelet transforms are used to evaluate the impacts of the different RIM configurations on the structure's natural frequencies when subjected to white noise loading. These measures for the structures with the VIRM are compared to the measures for the structures with the FIRM with slider masses locked at the initial location, FIRM (at x_0), and with the slider masses locked at R_{ubc}, FIRM (at R_{ubc}).

Figure 4 presents the ω_{IF} for the structures with different RIM configurations subject to white noise loading with different amplitudes. This figure shows that the ω_{IF} continuously vary for the structures with VIRM; this is due to the movement of the sliders in the VIRM flywheel during the response of the system. Figure 4 also shows that in all the cases, the ω_{IF} of the structures with VIRM are initially at its maximum and identical to the constant ω_{IF} of the structures with FIRM (at x_0), as expected due to the resting position of the slider masses. The range of variation in the ω_{IF} depend on the amplitude of the system loading and response. As the load amplitude increases, a decrease in the overall lower value of the ω_{IF_1} and ω_{IF_2} are observed for the structures with VIRM. For example, the minimum value of ω_{IF_2} for the 2VIRM structure is 4.91 Hz with white noise amplitude of 0.13 ms^{-2} and 2.77 Hz when the load amplitude is 1.03 ms^{-2}. At the low load amplitude of 0.13 ms^{-2}, although ω_{IF} is continuously shifting for both the 1VIRM and 2VIRM

structures, the ω_{IF} is closer to the 1FIRM (at x_0) and 2FIRM (at x_0), respectively. Furthermore, lower values of ω_{IF} are consistently observed for the 2VIRM structure, in comparison to the 1VIRM structure, at the two higher load amplitudes, particularly for ω_{IF_2}. This is due to the higher inertance ratio supplied from the attachment of the two VIRMs in the structure and aligns with research on inerters in MDOF structures [29], [49].

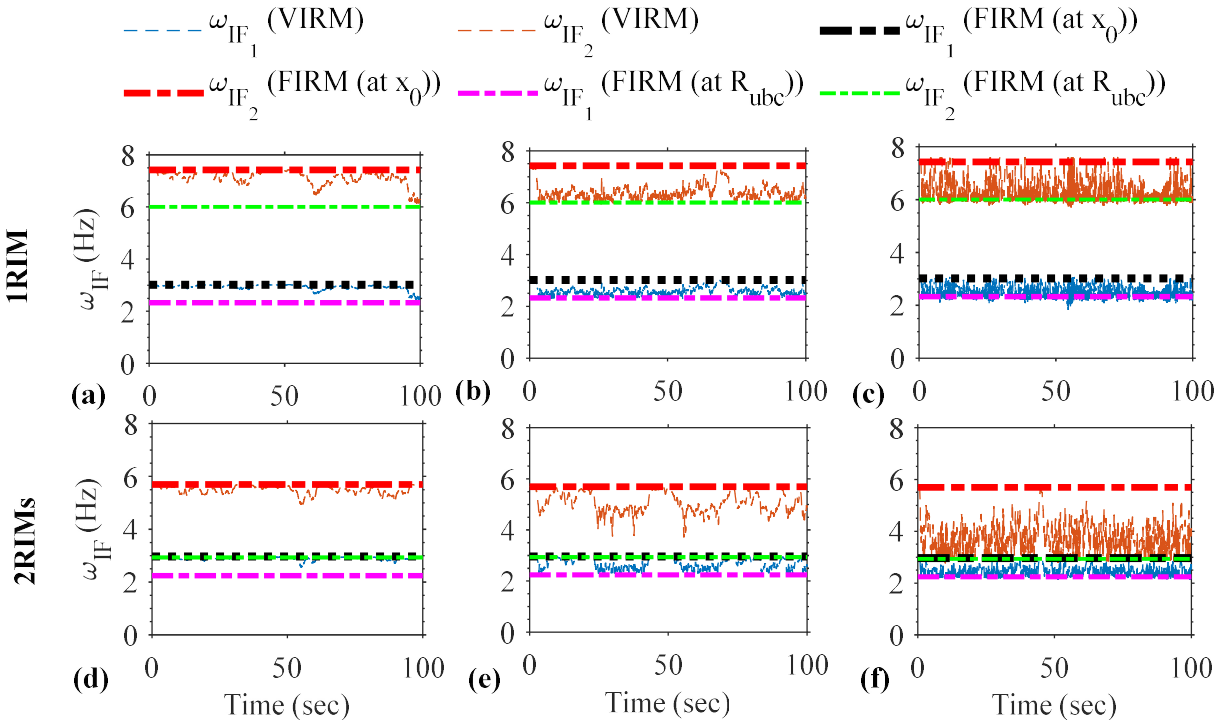

Figure 4. Instantaneous frequency of the structure with different RIM configurations (one RIM (a-c) and two RIMs (d-f)) with flywheel mass ratio of 0.008 under RMS white noise amplitudes: (a, d) 0.13 ms^{-2}, (b, e) 0.30 ms^{-2}, (c, f) 1.03 ms^{-2}

To investigate the effect of different RIM configurations and the load amplitude on the natural frequency shifts and the response of the primary structure, the story drifts and the wavelet transforms of those drifts are plotted in Figure 5. Note that, the relative displacement between the 2nd and 1st floors $\left(u_{s_2} - u_{s_1}\right)$ and between the 1st and ground floors $\left(u_{s_1} - u_g\right)$ are defined as the 2nd story drift and 1st story drift, respectively. Figure 5 shows the time-histories and wavelet

transformations of the 2nd story drift given the white noise loading with RMS amplitude of 1.03 ms^{-2}, which is the same loading considered in Figure 4c, f. It is observed in Figure 5a that the 2VIRM structure has the lowest 2nd story drift compared to other RIM structures. While Figure 5a also shows that the 1VIRM structure has an overall lower 2nd story drift time-history amplitude than the 1FIRM structure, the maximum drift amplitudes of both the configurations are more similar than the overall response.

Figure 5b, c, d, and e, depict the wavelet transforms of the 2nd story drift of the 2VIRM, 2FIRM, 1VIRM and 1FIRM structures, respectively. In these subplots, the darker shading indicates higher amplitude 2nd story drift response at the time and frequency of the shading. Furthermore, the different wavelet transforms in this figure are plotted such that a direct comparison of relative amplitude can be made when comparing the shading of the different subplots. The wavelet plots show an important 2nd mode response for the 1VIRM structure and a dominant 1st mode response for the 1FIRM and 2FIRM structures. In contrast, the 2VIRM structure shows a small 1st mode response and no noticeable distinct 2nd mode response. The reason for a missing distinct 2nd mode response is that, as seen in Figure 4f, the 2nd mode frequency of the 2VIRM structure has reduced to be, at times, nearly the same as the 1st mode frequency.

The influence of load amplitude on the natural frequency shifts can be investigated using the normalized weighted average instantaneous frequencies $\left(\Psi_{\varpi_{w_1}}, \Psi_{\varpi_{w_2}}\right)$ (see Figure 6 and Figure 7). These figures present the normalized weighted average instantaneous frequency, as defined in Section 3.2.1.3, versus the white noise RMS amplitude for different flywheel mass ratios. Figure 6 shows that the first mode normalized weighted average instantaneous frequency $\left(\Psi_{\varpi_{w_1}}\right)$ of the 1VIRM and 2VIRM structures closely match each other for the load amplitudes considered and

that $\Psi_{\varpi_{w1}}$ reduces as the load amplitude increases for both the 1VIRM and 2VIRM structures for all the flywheel mass ratios. As the FIRM structures are linear, their $\Psi_{\varpi_{w1}}$ does not vary with load amplitude. However, as the flywheel mass ratio increases, $\Psi_{\varpi_{w1}}$ decreases for both the structures with FIRM and VIRM. Additionally, $\Psi_{\varpi_{w1}}$ is slightly higher for the 1FIRM structure than the 2FIRM structure for all flywheel mass ratios.

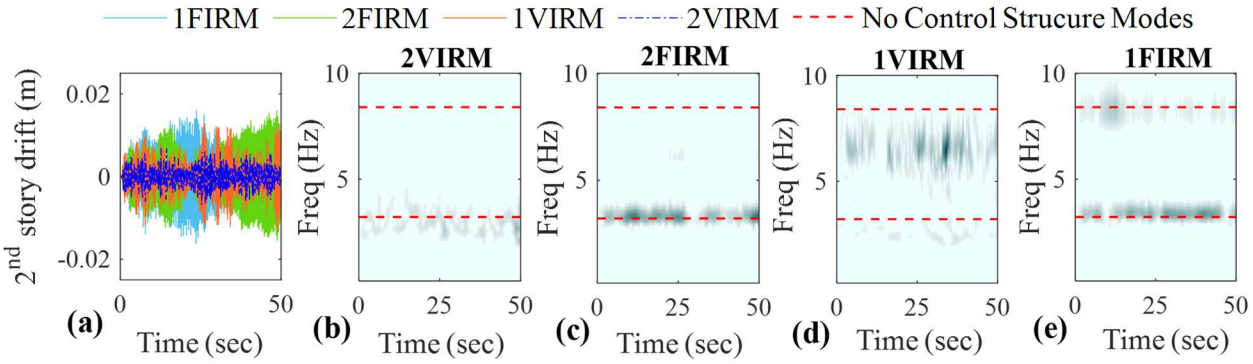

Figure 5. 2nd story drift and corresponding wavelet comparison of the structures with RIMs with a flywheel mass ratio 0.008 for a white noise RMS amplitude 1.03 ms^{-2}: (a) 2nd story drift, wavelet transform of (b) 2VIRM, (c) 2FIRM, (d) 1VIRM and (e) 1FIRM structures

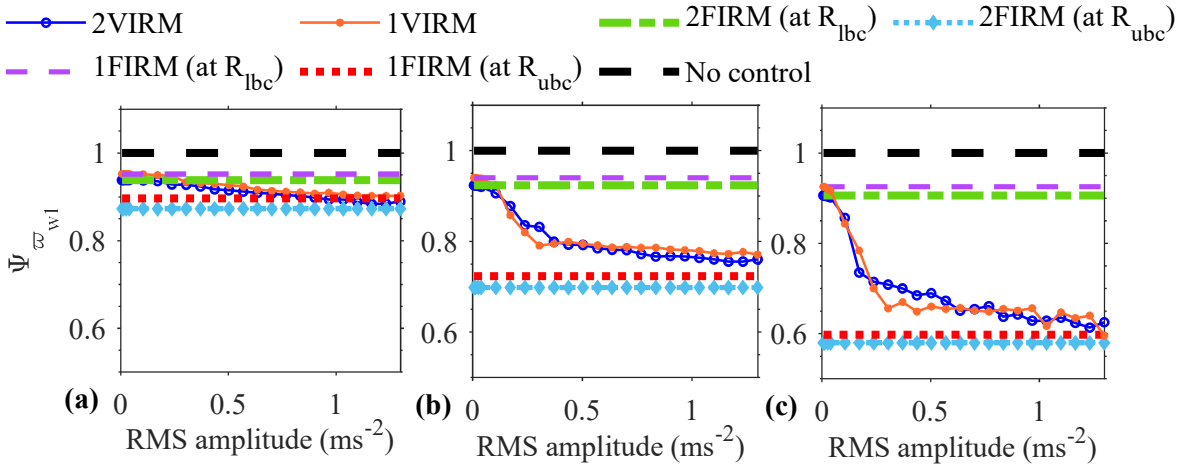

Figure 6. Normalized weighted average instantaneous frequency of the first mode, $\Psi_{\varpi_{w1}}$, of various RIM configurations, over a range of white noise amplitudes and for different flywheel mass ratios: (a) 0.003, (b) 0.008, and (c) 0.015

Figure 7 shows the second mode normalized weighted average instantaneous frequency $\left(\Psi_{\varpi_{w2}}\right)$ for different flywheel mass ratios and a range of white noise amplitudes. As with the $\Psi_{\varpi_{w1}}$ seen in Figure 6, the 1FIRM structure has a higher $\Psi_{\varpi_{w2}}$ than the 2FIRM structure; however, in the case of $\Psi_{\varpi_{w2}}$, the difference in this value between the 1FIRM and 2FIRM structures is large. Figure 7 shows that the 1VIRM structure has a significantly larger $\Psi_{\varpi_{w2}}$ compared to the 2VIRM structure; however, with the VIRM, the amplitude of $\Psi_{\varpi_{w2}}$ for both the 1VIRM and 2VIRM structures reduce with higher load amplitude.

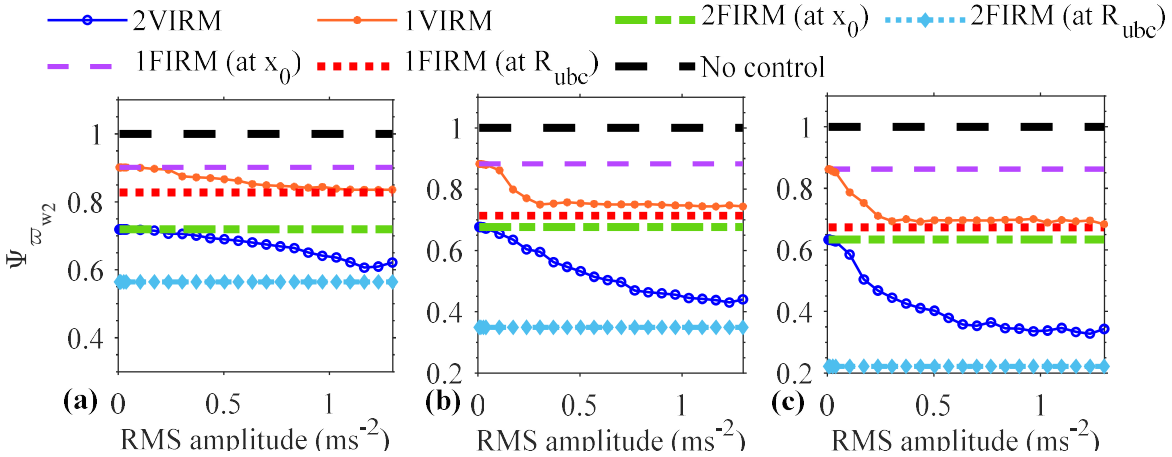

Figure 7. Normalized weighted average instantaneous frequency of the second mode, $\Psi_{\varpi_{w2}}$, of various RIM configurations, under a range of white noise amplitudes and for different flywheel mass ratios: (a) 0.003, (b) 0.008, and (c) 0.015

The results shown in this section demonstrate that, at a high enough amplitude of system response, a VIRM in the first story or VIRM in both stories can be used to shift both effective natural frequencies of the two-story structure examined. The resulting shifts in the 1st mode are similar for the 1VIRM or 2VIRM structures; however, the shifts in the 2nd mode are much less significant for the 1VIRM structure.

5 $\tilde{H}_2$ Response Measure

This section presents the results of the normalized $\tilde{H}_2$ measure, Σ, from the ground motion to story drift frequency response functions to investigate the performance of the VIRM in controlling the interstory displacement of the primary structure. This measure is evaluated for various amplitudes of white noise loading and different flywheel mass ratios.

The effect of flywheel mass ratios and the load amplitudes on the story drifts of the primary structure with different RIM configurations is presented in Figure 8. This figure shows that the performance of the structures with the FIRM remains unchanged as the loading amplitude increases, which is expected as the FIRM is linear. Note that, Σ of the structures with the FIRM is determined both when the slider masses are locked at x_0 and locked at R_{ubc}. While higher flywheel mass ratios reduce the overall natural frequency of the FIRM, Σ for the different FIRM configurations is sometimes less than one and sometimes more than one. This indicates that the effect of the FIRM on system performance is not always positive. As the FIRM only produces a constant effective mass and resulting change in system dynamics, it is believed that the change in Σ for the FIRM structures is mostly a result of the interaction of the specific time history of the finite duration white noise loading and the new shifted system dynamics. Furthermore, one can see that with the two larger flywheel mass ratios considered, the changes in performance of the FIRM are often much larger than for the smallest flywheel mass ratio. This is logical as the larger mass effects will produce larger shifts in the system dynamics and the resulting response will naturally have more dissimilarities to the response in the uncontrolled case.

Unlike for the structures with the FIRM, it is seen from the results in Figure 8 that Σ is always less than 1 for the structures with the VIRM. The Σ performance of the 1VIRM and 2VIRM structures are consistent at low load amplitudes, but increases in amplitude cause their

behavior to diverge. At higher load amplitudes, the Σ for the structures with the VIRM reduces and eventually reaches somewhat of a plateau with the 2VIRM structure always having a smaller value of Σ. As flywheel mass ratios increase, a distinct improvement in the performance of the structures with the VIRM is observed, resulting in lower minimum Σ values with higher flywheel mass ratios. The difference in results for the structures with VIRM and structures with FIRM help to illustrate that large mass effects are not alone sufficient to consistently mitigate response and that the nonlinear nature of the VIRM is an important factor in the overall superior performance shown here with the VIRM.

Both the 1VIRM and 2VIRM structures have similar performance at controlling the 1st story drift, but the 2VIRM configuration is better at reducing the 2nd story drift compared to the 1VIRM configuration. This is logical as the 1VIRM configuration does not include a VIRM in the second story. Similarly, the absence of a FIRM in the second story in the 1FIRM structure coincides with poor performance in reducing the 2nd story drift.

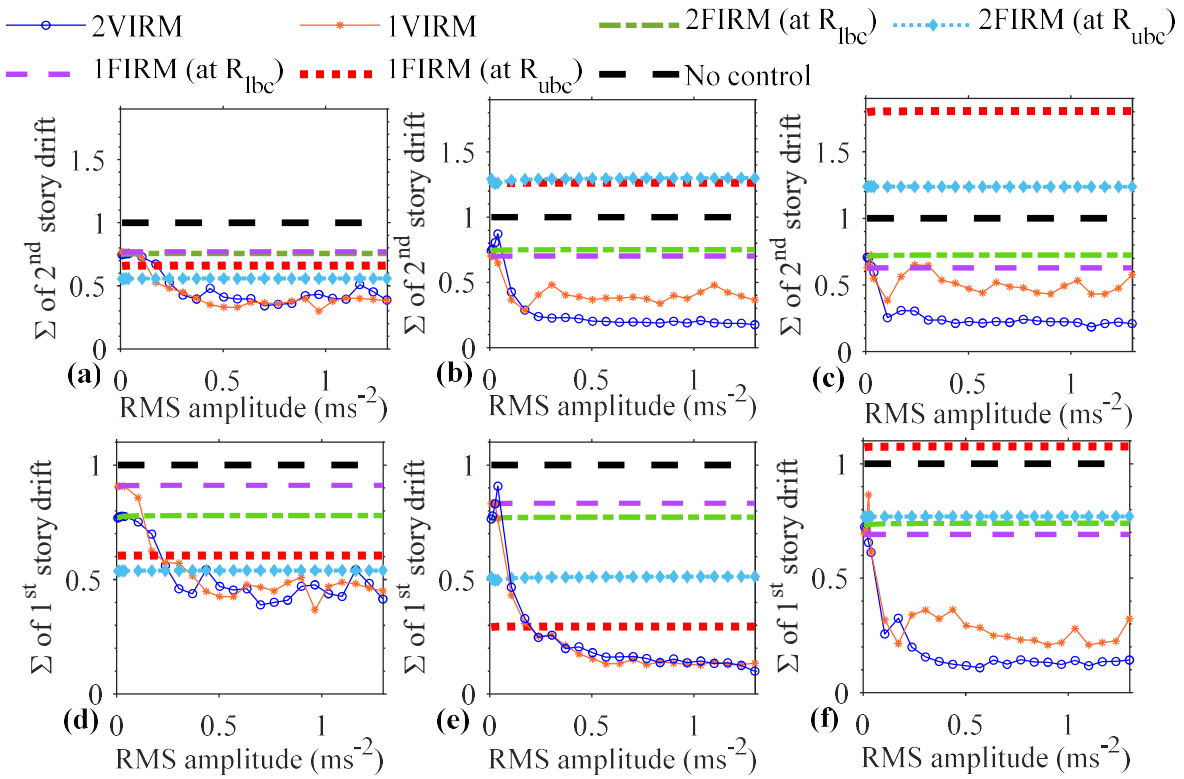

Figure 8. Normalized $\tilde{H}_2$, Σ, of the 2nd story drift and 1st story drift of the primary structure with RIMs of different flywheel mass ratios: (a,d) 0.003, (b,e) 0.008, and (c,f) 0.015, over a range of white noise RMS amplitudes.

Considering a pair of flywheel mass ratios, the influence of RIMs on the frequency response function (FRF) curves of the ground excitation to the primary structure's 2nd and 1st story drifts are depicted in Figure 9. Additionally, the frequency response curve for the no control case is included for reference. The peaks of the FRFs in this figure are utilized to discuss the system natural frequencies, including changes in peak frequency and amplitude, highlighting the overall impact of RIMs on the FRF curves. As the FIRM possesses linear properties, the FRFs for the FIRM structures are characterized by smooth curves. In contrast, the nonlinear behavior of the VIRMs results in non-smooth FRF curves for the VIRM structures.

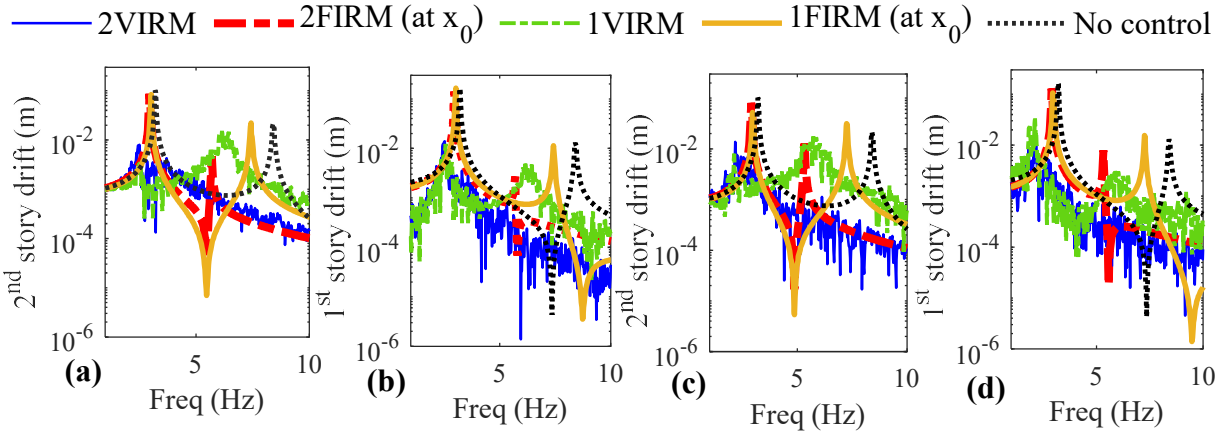

Figure 9. Frequency response curves of 2nd story and 1st story drift under a normalized RMS white noise amplitude of 0.30 ms^{-2} for different structural configurations with RIM flywheel mass ratios: (a-b) 0.008, and (c-d) 0.015

Figure 9, as expected, shows that all of the RIMs lead to reductions in the effective system frequencies seen in the FRFs compared to the no control structure. These reductions in frequencies are more pronounced for the structures with VIRM than the structures with FIRM. The figure also shows that for the 2VIRM structure there appears to be only one dominant effective frequency, the 1st mode frequency. In both story drifts, the 1st mode peak amplitude of the 1VIRM structure is similar to the 2VIRM structure for both flywheel mass ratios considered; however, the 1VIRM structure also has a distinct 2nd mode with a significant peak in the FRF. This high 2nd mode peak amplitude of the 1VIRM structure is the reason for its larger H_2 response measure, as shown in Figure 8.

6 Incremental Dynamic Analysis

This section presents the findings of a parametric incremental dynamic analysis (IDA) of the 2DOF structure subjected to the suite of considered ground motions across a range of spectral intensity, S_T, values. Different RIM configurations and flywheels with various sizes of slider masses are considered in this analysis.

An example of the interstory displacement time-history responses from one ground motion at one spectral intensity for one set of flywheel slider masses is shown in Figure 10. In this section, the resulting response over the suite of ground motions at each spectral intensity is used to calculate two measures to evaluate the response of the systems, the maximum absolute story drift (MASD) and the maximum absolute story acceleration (MASA). These measures for the structures with RIM configurations are normalized against the no control case and median normalized MASD and MASA values are determined for multiple ground motions.

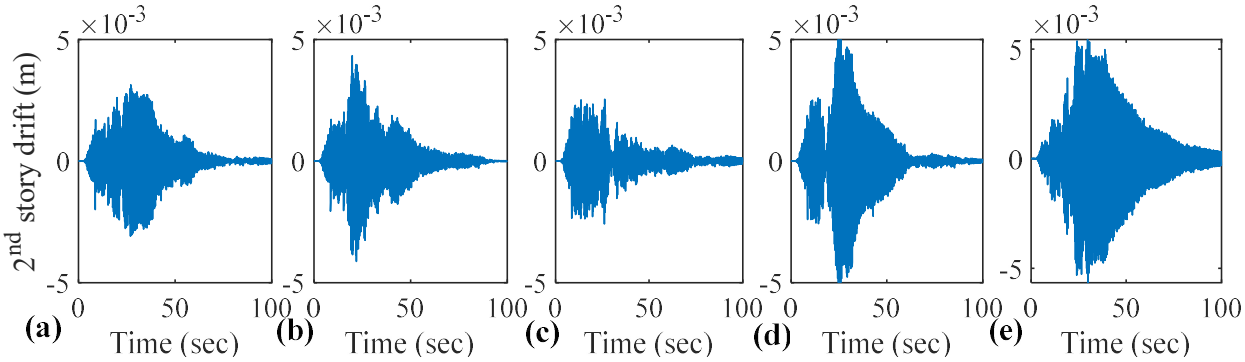

Figure 10. Time history of 2nd story drift for the different structure configurations: (a) 2VIRM, (b) 2FIRM, (c) 1VIRM, (d) 1FIRM, and (e) No control, under Kobe earthquake at a spectral intensity of 1 ms^{-2}. The RIM structures have a flywheel mass ratio of 0.008

Figure 11 shows the resulting S_T vs MASD curves from the IDAs of the 2DOF structure with different RIM configurations. Each single line represents results for a specific ground motion scaled with increasing spectral intensity. Differences between the lines indicate the differences in response when subjected to different ground motions given each ground motion's unique temporal and frequency characteristics. As the FIRM structures are linear, the MASD increases linearly with increasing scaled amplitude for individual earthquake records. For the 1VIRM and 2VIRM structures, the IDA curves exhibit an initially linear response when the ground motion intensity is low. During these low intensities, the sliders in the VIRM remain very close to the initial positions, resulting in behavior resembling that of the 1FIRM and 2FIRM structures (at x_0). However, as the

ground motion intensity increases, the slider masses have more significant radial motion, leading to a nonlinear response that causes the IDA curves for the 1VIRM and 2VIRM structures to deviate from the initial linear segments. As the ground motion intensity increases, the MASD generally exhibits an increasing trend for the VIRM structures, although not necessarily monotonically. The median response for each configuration across all seismic records at each intensity level, as depicted in Figure 11, shows the overall trend from the IDA results.

The median normalized MASD IDA curves for RIM configurations with different flywheel mass ratios and the no control case are presented in Figure 12. Due to the normalization, x-axis values below one indicate the RIM's effectiveness in mitigating structural response compared to the no control structure. The shaded region of the plots represents the median absolute deviation (MAD) of the normalized response. The vertical normalized curves for the structures with FIRM signify that the ground motion intensity does not impact the effectiveness of the linear FIRM. At the lower flywheel mass ratio of 0.003, the 1FIRM structure has a lower median response than the 2VIRM structure. However, as the flywheel mass ratio increases, the 2FIRM structure has a lower median response than the 1FIRM structure. Figure 12 shows that at low spectral intensities, the 2VIRM structure is more effective than the 1VIRM structure at reducing the median MASD. However, as the spectral intensity increases, the 2VIRM and 1VIRM structures show similar performance in terms of reducing the maximum absolute story drift. The figure also shows that the increase in flywheel mass ratios reduces the median normalized MASD response of the structures with VIRM and FIRM.

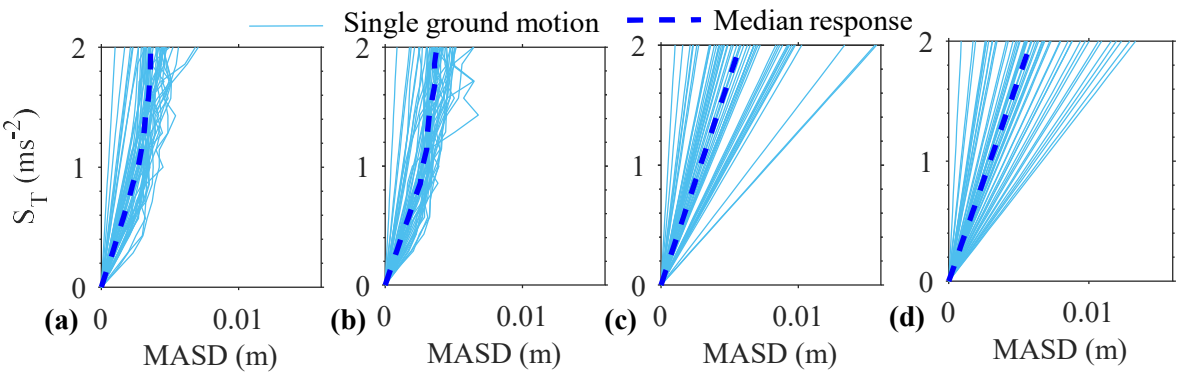

Figure 11. IDA curves showing spectral acceleration (S_T) vs maximum absolute story drift (MASD) of the (a) 2VIRM, (b) 1VIRM, (c) 2FIRM, and (d) 1FIRM structures, with a flywheel mass ratio of 0.008

In addition to drift performance, another important parameter to consider is the impact of these devices on the acceleration response of the structures. Figure 13 presents the median normalized MASA for the RIM configurations with different flywheel mass ratios and no control structure. Similar trends are observed for the median normalized MASA as the median normalized MASD for the FIRM structures which shows that the 2FIRM structure has lower median response than the 1FIRM structure at the higher flywheel mass ratios and the opposite for the lowest flywheel mass ratios considered. While the normalized median response for the 2FIRM structure reduces as the flywheel mass ratios increase, the normalized median response for the 1FIRM structure changes much less significantly. In the low flywheel mass ratio case, both the 1VIRM and 2VIRM structures were more effective in reducing story acceleration than their counterparts with FIRM at higher intensities. The performance of the 2VIRM structure seen in this figure is also comparable to the normalized MASD performance shown in Figure 12.

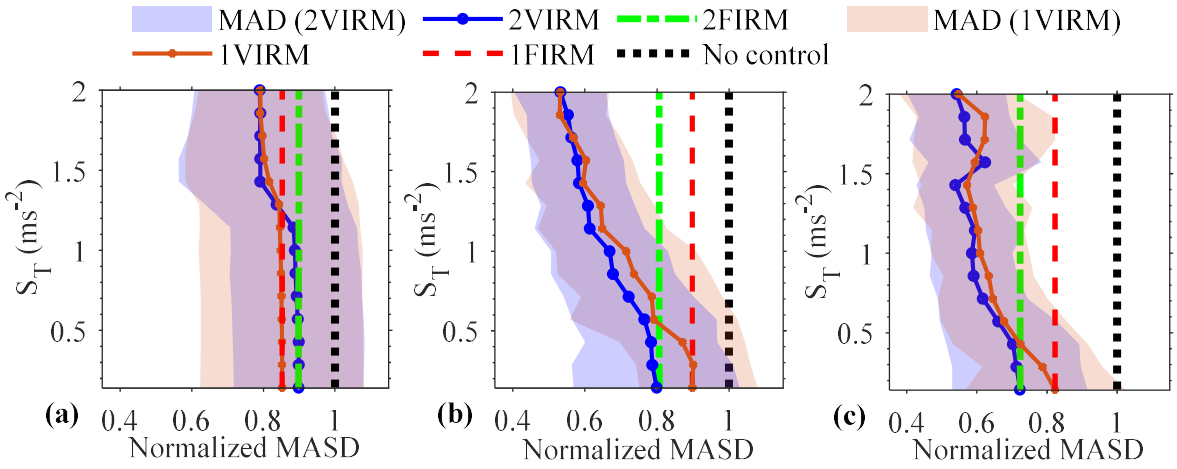

Figure 12. S_T vs median normalized MASD IDA curves considering the different RIM configurations and flywheel mass ratios (a) 0.003, (b) 0.008, and (c) 0.015

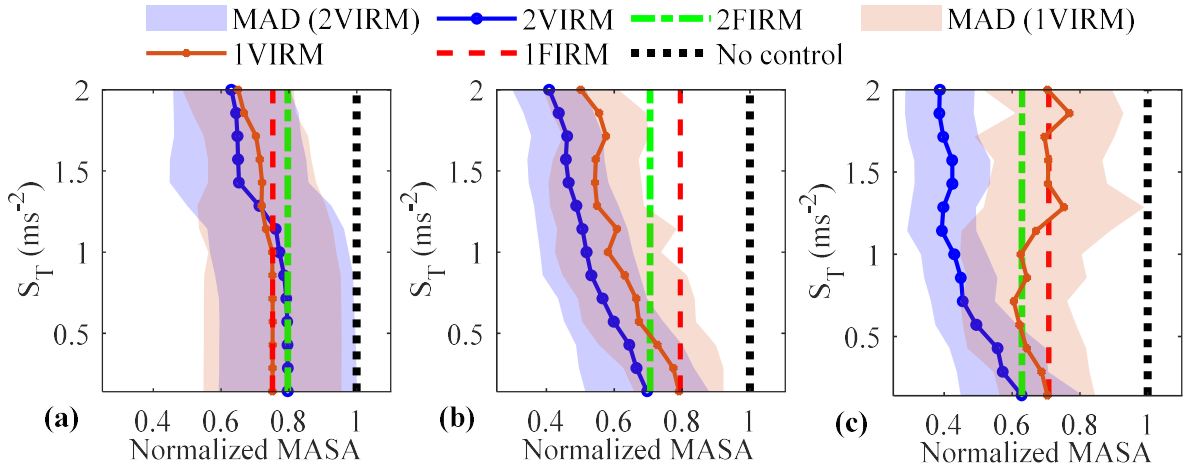

Figure 13. S_T vs median normalized MASA IDA curves considering the different RIM configurations and flywheel mass ratios (a) 0.003, (b) 0.008, and (c) 0.015

The most notable difference in the MASA results shown in Figure 13 compared to the MASD results shown in Figure 12 is the performance of the 1VIRM structure. While the 1VIRM structure exhibits comparable performance to the 2VIRM structure in reducing normalized maximum absolute story drifts, it is significantly less effective in reducing normalized maximum absolute acceleration as the flywheel mass ratio increases. At a flywheel mass ratio of 0.015, there are multiple instances where the normalized median MASA of the 1VIRM structure approaches and occasionally exceeds that of the 1FIRM structure. The poor performance of the 1VIRM

structure at higher flywheel mass ratios in terms of acceleration response, compared to other RIM configurations, is likely because the 1VIRM structure was shown to be largely ineffective at reducing the higher mode response.

7 Conclusion

This study investigates the use of a variable inertia rotational mechanism (VIRM) for the passive vibration control of a multi-degree-of-freedom structure subjected to base excitation. The study examines the response of a 2DOF structure, in which the VIRM is employed in two configurations: (a) in the 2VIRM structure, one VIRM is employed between the ground and 1st floor and another VIRM is employed between the 1st and the 2nd floor and (b) in the 1VIRM structure, only one VIRM, positioned between the ground and the 1st floor, is employed. Similar structures with fixed inertia rotational mechanisms (FIRM) are also examined in this study to draw comparisons with the structures with VIRM. The equations of motion of the different structural configurations are formulated and described. The natural frequency and $\tilde{H}_2$ response measures were assembled from the time-history analysis of the structure under white noise base loading. Incremental dynamic analyses were performed to evaluate the maximum absolute story displacement and maximum absolute acceleration response given a suite of seismic ground motions. The following key results were observed from this study.

- The effective natural frequency of the structures with a VIRM depends on the load amplitude and flywheel mass ratios. Higher flywheel mass ratios or load intensities led to decreases in effective natural frequencies for both the 1VIRM and 2VIRM structures.
- The 2VIRM structure was found to be much more effective than the 1VIRM structure at reducing the effective second mode natural frequency.

- The performance of the VIRM in response mitigation is strongly influenced by the intensity of the loading. At low load intensities, VIRMs and FIRMs (slider masses fixed at initial positions) have a similar impact on the responses of the structures. At higher load intensities, improved response reduction is observed for the structures with VIRM, especially the 2VIRM structure.
- Higher flywheel mass ratios contribute to enhanced performance at reducing story drifts for the 2VIRM and 1VIRM structures; however, the 1VIRM structure performance deteriorated at reducing story accelerations with increasing flywheel mass ratios.
- Although a single VIRM can have a large impact on the response of the structure, to effectively mitigate the response at each story and in each mode, VIRMs would be needed at each story.

The exploration of the VIRM's behavior and its impact on frequency shifts and structural response done in this study presents a compelling case for its efficacy in structural control. Some of the results of these study would be likely true for more complex structures, such as the relative advantages of distributing VIRM rather than concentrating at a particular story; however, it is unclear how the performance of the VIRM would change in a more modally rich environment. Further parametric investigation of the VIRM as a passive control device for structures under diverse loading scenarios and considering more realistic models of structures is imperative for further evaluating the effectiveness of the VIRM.

Acknowledgements

This research is based upon work supported by the National Science Foundation under Grant No. 1944513. Any opinions, findings, and conclusions or recommendations expressed in this material are those of the authors and do not necessarily reflect the views of the National Science Foundation.

References

[1] J. M. Kelly, *Earthquake-Resistant Design with Rubber*. London: Springer London, 1993.
[2] J. M. Kelly, R. I. Skinner, and A. J. Heine, "Mechanisms of energy absorption in special devices for use in earthquake resistant structures," *Bull. N. Z. Soc. Earthq. Eng.*, vol. 5, no. 3, pp. 63–88, Sep. 1972, doi: 10.5459/bnzsee.5.3.63-88.
[3] T. T. Soong and M. C. Costantinou, Eds., *Passive and Active Structural Vibration Control in Civil Engineering*, vol. 345. in CISM International Centre for Mechanical Sciences, vol. 345. Vienna: Springer Vienna, 1994. doi: 10.1007/978-3-7091-3012-4.
[4] T. T. Soong and G. F. Dargush, *Passive energy dissipation systems in structural engineering*. Chichester ; New York: Wiley, 1997.
[5] R. I. Skinner, W. H. Robinson, and G. H. McVerry, *An introduction to seismic isolation*. Chichester ; New York: Wiley, 1993.
[6] T. Arakaki, H. Kuroda, F. Arima, Y. Inoue, and K. Baba, "DEVELOPMENT OF SEISMIC DEVICES APPLIED TO BALL SCREW : Part 1 Basic performance test of RD-series," *AIJ J. Technol. Des.*, vol. 5, no. 8, pp. 239–244, 1999, doi: 10.3130/aijt.5.239_1.
[7] M. C. Smith, "Synthesis of mechanical networks: the inerter," *IEEE Trans. Autom. Control*, vol. 47, no. 10, pp. 1648–1662, Oct. 2002, doi: 10.1109/TAC.2002.803532.
[8] Y. Sugimura, Goto, W., Saito, K., Nimomiya, T., and Tanizawa, H., "Sugimura, Y., Goto, W., Tanizawa, H., Saito, K. and Nimomiya, T., 2012, September. Response control effect of steel building structure using tuned viscous mass damper. In Proceedings of the 15th world conference on earthquake engineering (Vol. 9, pp. 24-28).," 2012, pp. 24–28.
[9] K. Ikago, K. Saito, and N. Inoue, "Seismic control of single-degree-of-freedom structure using tuned viscous mass damper: THE TUNED VISCOUS MASS DAMPER," *Earthq. Eng. Struct. Dyn.*, vol. 41, no. 3, pp. 453–474, Mar. 2012, doi: 10.1002/eqe.1138.
[10] A. Javidialesaadi and N. E. Wierschem, "Energy transfer and passive control of single-degree-of-freedom structures using a one-directional rotational inertia viscous damper," *Eng. Struct.*, vol. 196, p. 109339, Oct. 2019, doi: 10.1016/j.engstruct.2019.109339.
[11] T. Arakaki, H. Kuroda, F. Arima, Y. Inoue, and K. Baba, "DEVELOPMENT OF SEISMIC DEVICES APPLIED TO BALL SCREW : Part 2 Performance test and evaluation of RD-series," *AIJ J. Technol. Des.*, vol. 5, no. 9, pp. 265–270, 1999, doi: 10.3130/aijt.5.265.
[12] D. De Domenico, G. Ricciardi, and R. Zhang, "Optimal design and seismic performance of tuned fluid inerter applied to structures with friction pendulum isolators," *Soil Dyn. Earthq. Eng.*, vol. 132, p. 106099, May 2020, doi: 10.1016/j.soildyn.2020.106099.
[13] M. C. Smith, "FORCE-CONTROLLING MECHANICAL DEVICE," US 7,316, 303 B2, Jan. 08, 2008
[14] M. C. Smith, "Force-Controlling Hydraulic Device," US 2021/0199428 A1, Aug. 09, 2012
[15] S. J. Swift, M. C. Smith, A. R. Glover, C. Papageorgiou, B. Gartner, and N. E. Houghton, "Design and modelling of a fluid inerter," *Int. J. Control*, vol. 86, no. 11, pp. 2035–2051, Nov. 2013, doi: 10.1080/00207179.2013.842263.
[16] M. Chen, C. Papageorgiou, F. Scheibe, F. Wang, and M. Smith, "The missing mechanical circuit element," *IEEE Circuits Syst. Mag.*, vol. 9, no. 1, pp. 10–26, 2009, doi: 10.1109/MCAS.2008.931738.
[17] A. Kuznetsov, M. Mammadov, I. Sultan, and E. Hajilarov, "Optimization of improved suspension system with inerter device of the quarter-car model in vibration analysis," *Arch. Appl. Mech.*, vol. 81, no. 10, pp. 1427–1437, Oct. 2011, doi: 10.1007/s00419-010-0492-x.

[18] A. Giaralis and F. Petrini, "Wind-Induced Vibration Mitigation in Tall Buildings Using the Tuned Mass-Damper-Inerter," *J. Struct. Eng.*, vol. 143, no. 9, p. 04017127, Sep. 2017, doi: 10.1061/(ASCE)ST.1943-541X.0001863.
[19] D. Pietrosanti, M. De Angelis, and M. Basili, "Optimal design and performance evaluation of systems with Tuned Mass Damper Inerter (TMDI): Optimal Design and Performance of Tuned Mass Damper Inerter Systems," *Earthq. Eng. Struct. Dyn.*, vol. 46, no. 8, pp. 1367–1388, Jul. 2017, doi: 10.1002/eqe.2861.
[20] A. Di Egidio, S. Pagliaro, and C. Fabrizio, "Combined Use of Rocking Walls and Inerters to Improve the Seismic Response of Frame Structures," *J. Eng. Mech.*, vol. 147, no. 5, p. 04021016, May 2021, doi: 10.1061/(ASCE)EM.1943-7889.0001920.
[21] J.-S. Hwang, J. Kim, and Y.-M. Kim, "Rotational inertia dampers with toggle bracing for vibration control of a building structure," *Eng. Struct.*, vol. 29, no. 6, pp. 1201–1208, Jun. 2007, doi: 10.1016/j.engstruct.2006.08.005.
[22] Z. Zhao, R. Zhang, Y. Jiang, and C. Pan, "Seismic response mitigation of structures with a friction pendulum inerter system," *Eng. Struct.*, vol. 193, pp. 110–120, Aug. 2019, doi: 10.1016/j.engstruct.2019.05.024.
[23] H. Gao, H. Wang, J. Li, J. Mao, and Z. Wang, "Dynamic behavior and damping enhancement of cable with negative stiffness inerter damper," *Int. J. Mech. Sci.*, vol. 235, p. 107664, Dec. 2022, doi: 10.1016/j.ijmecsci.2022.107664.
[24] H. Gao *et al.*, "Optimum design of viscous inerter damper targeting multi-mode vibration mitigation of stay cables," *Eng. Struct.*, vol. 226, p. 111375, Jan. 2021, doi: 10.1016/j.engstruct.2020.111375.
[25] A. Giaralis and A. A. Taflanidis, "Optimal tuned mass-damper-inerter (TMDI) design for seismically excited MDOF structures with model uncertainties based on reliability criteria," *Struct. Control Health Monit.*, vol. 25, no. 2, p. e2082, Feb. 2018, doi: 10.1002/stc.2082.
[26] A. Javidialesaadi and N. E. Wierschem, "Optimal design of rotational inertial double tuned mass dampers under random excitation," *Eng. Struct.*, vol. 165, pp. 412–421, Jun. 2018, doi: 10.1016/j.engstruct.2018.03.033.
[27] D. De Domenico and G. Ricciardi, "Optimal design and seismic performance of tuned mass damper inerter (TMDI) for structures with nonlinear base isolation systems," *Earthq. Eng. Struct. Dyn.*, Aug. 2018, doi: 10.1002/eqe.3098.
[28] Q. Wang, H. Qiao, D. De Domenico, Z. Zhu, and Z. Xie, "Wind-Induced Response Control of High-Rise Buildings Using Inerter-Based Vibration Absorbers," *Appl. Sci.*, vol. 9, no. 23, p. 5045, Nov. 2019, doi: 10.3390/app9235045.
[29] M. Z. Q. Chen, Y. Hu, L. Huang, and G. Chen, "Influence of inerter on natural frequencies of vibration systems," *J. Sound Vib.*, vol. 333, no. 7, pp. 1874–1887, Mar. 2014, doi: 10.1016/j.jsv.2013.11.025.
[30] L. Marian and A. Giaralis, "Optimal design of a novel tuned mass-damper–inerter (TMDI) passive vibration control configuration for stochastically support-excited structural systems," *Probabilistic Eng. Mech.*, vol. 38, pp. 156–164, Oct. 2014, doi: 10.1016/j.probengmech.2014.03.007.
[31] I. F. Lazar, S. A. Neild, and D. J. Wagg, "Using an inerter-based device for structural vibration suppression: USING AN INERTER-BASED DEVICE FOR STRUCTURAL VIBRATION SUPPRESSION," *Earthq. Eng. Struct. Dyn.*, vol. 43, no. 8, pp. 1129–1147, Jul. 2014, doi: 10.1002/eqe.2390.

[32] D. De Domenico, H. Qiao, Q. Wang, Z. Zhu, and G. Marano, "Optimal design and seismic performance of Multi-Tuned Mass Damper Inerter (MTMDI) applied to adjacent high-rise buildings," *Struct. Des. Tall Spec. Build.*, Jun. 2020, doi: 10.1002/tal.1781.
[33] Q. Wang, H. Qiao, D. De Domenico, Z. Zhu, and Y. Tang, "Seismic performance of optimal Multi-Tuned Liquid Column Damper-Inerter (MTLCDI) applied to adjacent high-rise buildings," *Soil Dyn. Earthq. Eng.*, vol. 143, p. 106653, Apr. 2021, doi: 10.1016/j.soildyn.2021.106653.
[34] F. de H. Moraes, M. Silveira, and P. J. P. Gonçalves, "On the dynamics of a vibration isolator with geometrically nonlinear inerter," *Nonlinear Dyn.*, vol. 93, no. 3, pp. 1325–1340, Aug. 2018, doi: 10.1007/s11071-018-4262-6.
[35] Y. Wang, H.-X. Li, C. Cheng, H. Ding, and L.-Q. Chen, "A nonlinear stiffness and nonlinear inertial vibration isolator," *J. Vib. Control*, vol. 27, no. 11–12, pp. 1336–1352, Jun. 2021, doi: 10.1177/1077546320940924.
[36] Y. Wang, R. Wang, H. Meng, and B. Zhang, "An investigation of the dynamic performance of lateral inerter-based vibration isolator with geometrical nonlinearity," *Arch. Appl. Mech.*, vol. 89, no. 9, pp. 1953–1972, Sep. 2019, doi: 10.1007/s00419-019-01554-9.
[37] X. Dong, J. Xi, P. Chen, and W. Li, "Magneto-rheological variable inertia flywheel," *Smart Mater. Struct.*, vol. 27, no. 11, p. 115015, Nov. 2018, doi: 10.1088/1361-665X/aad42b.
[38] Y. Zhang, X. Zhang, T. Qian, and R. Hu, "Modeling and simulation of a passive variable inertia flywheel for diesel generator," *Energy Rep.*, vol. 6, pp. 58–68, Dec. 2020, doi: 10.1016/j.egyr.2020.01.001.
[39] J. Yang, J. Z. Jiang, and S. A. Neild, "Dynamic analysis and performance evaluation of nonlinear inerter-based vibration isolators," *Nonlinear Dyn.*, vol. 99, no. 3, pp. 1823–1839, Feb. 2020, doi: 10.1007/s11071-019-05391-x.
[40] T. Xu, M. Liang, C. Li, and S. Yang, "Design and analysis of a shock absorber with variable moment of inertia for passive vehicle suspensions," *J. Sound Vib.*, vol. 355, pp. 66–85, Oct. 2015, doi: 10.1016/j.jsv.2015.05.035.
[41] S. Yang, T. Xu, C. Li, M. Liang, and N. Baddour, "Design, Modeling and Testing of a Two-Terminal Mass Device With a Variable Inertia Flywheel," *J. Mech. Des.*, vol. 138, no. 9, p. 095001, Sep. 2016, doi: 10.1115/1.4034174.
[42] A. C. Mahato, S. K. Ghoshal, and A. K. Samantaray, "Influence of variable inertia flywheel and soft switching on a power hydraulic system," *SN Appl. Sci.*, vol. 1, no. 6, p. 605, Jun. 2019, doi: 10.1007/s42452-019-0623-0.
[43] P. Kushwaha, S. K. Ghoshal, and K. Dasgupta, "Dynamic analysis of a hydraulic motor drive with variable inertia flywheel," *Proc. Inst. Mech. Eng. Part J. Syst. Control Eng.*, vol. 234, no. 6, pp. 734–747, Jul. 2020, doi: 10.1177/0959651819875914.
[44] Q. Li, X. Li, J. Mi, B. Jiang, S. Chen, and L. Zuo, "Tunable Wave Energy Converter Using Variable Inertia Flywheel," *IEEE Trans. Sustain. Energy*, vol. 12, no. 2, pp. 1265–1274, Apr. 2021, doi: 10.1109/TSTE.2020.3041664.
[45] C. Jauch, "A flywheel in a wind turbine rotor for inertia control," *Wind Energy*, vol. 18, no. 9, pp. 1645–1656, Sep. 2015, doi: 10.1002/we.1784.
[46] D. G. Ullman, "A variable inertia flywheel as an energy storage system," The Ohio State University, 1978.
[47] MathWorks, "MATLAB: Mathematics (R2022a)." Accessed: Aug. 15, 2022. [Online]. Available: https://www.mathworks.com/help/pdf_doc/matlab/matlab_math.pdf

[48] U.S. Department Security and Federal Emergency Agency, "Quantification of Building Seismic Performance Factors (FEMA P695/ June 2009)," 2009.
[49] Y. Wen, F. Gomez, D. Li, and B. F. Spencer, "Generalized optimal design of multiple tuned inerter dampers for control of MDOF structures under stochastic seismic excitation," *Struct. Control Health Monit.*, vol. 29, no. 1, Jan. 2022, doi: 10.1002/stc.2853.

Appendix

The parameter notations of the system properties are presented in Section 2. The equation of motion of the system can be obtained using Lagrange's equation, The Lagrangian, L, is defined as

$$L = T - V \tag{A.1}$$

where T and V are the kinetic and potential energy of the system, respectively. The kinetic energy is the contribution of the structure motion, rotational velocity of the VIRM flywheel and the slider mass velocities. The potential energy is the energy stored in the structure's springs, and the VIRM's nonlinear spring. The gravitational effect on the VIRM slider movement is not considered in this derivation. While gravity would have no impact on a horizontally positioned flywheel, it is an open question if the gravitational effect on a VIRM with a vertically positioned flywheel would be important. The potential energy of the VIRM trilinear springs can be expressed as

$$V_{sd_i} = \begin{cases} n_i \frac{1}{2} k_{sd} \left(R_{lbc} - x_0\right)^2 + n_i \frac{1}{2} k_p \left(x_i - R_{lbc}\right)^2 + n_i k_{sd} \left(R_{lbc} - x_0\right)\left(x_i - R_{lbc}\right); x_i < R_{lbc} \\ n_i \frac{1}{2} k_{sd} \left(x - x_0\right)^2 ; R_{lbc} \le x_i < R_{ubc} \\ n_i \frac{1}{2} k_{sd} \left(R_{ubc} - x_0\right)^2 + n_i \frac{1}{2} k_p \left(x_i - R_{ubc}\right)^2 + n_i k_{sd} \left(R_{ubc} - x_0\right)\left(x_i - R_{ubc}\right); x_i \ge R_{ubc} \end{cases} \tag{A.2}$$

Here, *i* presents the VIRM attachment at the i[th] story. In the 2VIRM configuration, there will be two potential energies, $\left(V_{sd_1}, V_{sd_2}\right)$, from the two VIRMs at each story. As this potential energy depends on the radial position of the slider masses, there could be a total of nine pairs of V_{sd_1} and

V_{sd_2} expressions between the two VIRMs. The kinetic energy, potential energy, and the virtual work of the non-conservative forces, ∂W_{NC} , of the 2VIRM structure is formulated as

$$T = \frac{1}{2} m_{s_1} \left(\dot{u}_{s_1} + \dot{u}_g \right)^2 + \frac{1}{2} m_{s_2} \left(\dot{u}_{s_2} + \dot{u}_g \right)^2 + \frac{1}{2} J_{\mathrm{VIRM}_1} \dot{\theta}_1^{\,2} + \frac{1}{2} J_{\mathrm{VIRM}_2} \dot{\theta}_2^{\,2} + n_1 \frac{1}{2} m_{sd_1} \dot{x}_1^{\,2} + n_2 \frac{1}{2} m_{sd_2} \dot{x}_2^{\,2} \quad \text{(A.3)}$$

$$V = \frac{1}{2} k_{s_1} \left(u_{s_1} - u_g \right)^2 + \frac{1}{2} k_{s_2} \left(u_{s_2} - u_{s_1} \right)^2 + V_{sd_1} \left(x_1 \right) + V_{sd_2} \left(x_2 \right) \quad \text{(A.4)}$$

$$W_{NC} = \left(c_{s_2} \dot{u}_{s_2} - \left(c_{s_1} + c_{s_2} \right) \dot{u}_{s_1} + c_{s_1} \dot{u}_g \right) \partial u_{s_1} + \left(c_{s_2} \dot{u}_{s_1} - c_{s_2} \dot{u}_{s_2} + P(t) \right) \partial u_{s_2} - n_1 c_{sd_1} \dot{x}_1 \partial x_1 - n_2 c_{sd_2} \dot{x}_2 \partial x_2 \quad \text{(A.5)}$$

The multiple slider masses in a VIRM are assumed to be moving synchronously with the same radial motion.

Lagrange's equation for the structure in generalized coordinates is given as

$$\frac{d}{dt} \frac{\partial \mathrm{T}}{\partial \dot{q}_i} - \frac{\partial \mathrm{T}}{\partial q_i} + \frac{\partial V}{\partial q_i} = p_i(t), \; i = 1, 2, 3, 4; \quad \text{(A.6)}$$

where q_1, q_2, q_3, q_4 are the displacements relative to the ground of the two masses of the primary structure (u_{s_1} and u_{s_2}) and the radial displacements of the slider masses in the two VIRMs (x_1 and x_2); T and V denote the kinetic energy and potential energy of the dynamic system, respectively. The resulting equations of motion can be expressed as

$$\begin{aligned}
&m_{s_1} \ddot{u}_{s_1} + J_{VIRM_1} \alpha^2 \left(\ddot{u}_{s_1} - \ddot{u}_g \right) - J_{VIRM_2} \alpha^2 \left(\ddot{u}_{s_2} - \ddot{u}_{s_1} \right) + \left(2 n_1 m_{sd} x_1 \alpha^2 \dot{u}_{s_1} \right) \dot{x}_1 - \left(2 n_2 m_{sd} x_2 \alpha^2 \left(\dot{u}_{s_2} - \dot{u}_{s_1} \right) \right) \dot{x}_2 \\
&+ \left(c_{s_2} + c_{s_1} \right) \dot{u}_{s_1} - c_{s_2} \dot{u}_{s_2} - c_{s_1} \dot{u}_g + \left(k_{s_1} + k_{s_2} \right) u_{s_1} - k_{s_2} u_{s_2} - k_{s_1} u_g = -m_{s_1} \ddot{u}_g \\
&m_{s_2} \ddot{u}_{s_2} + J_{VIRM_2} \alpha^2 \left(\ddot{u}_{s_2} - \ddot{u}_{s_1} \right) + 2 n_2 m_{sd} x_2 \alpha^2 \left(\dot{u}_{s_2} - \dot{u}_{s_1} \right) \dot{x}_2 + k_{s_2} \left(u_{s_2} - u_{s_1} \right) - c_{s_2} \dot{u}_{s_1} + c_{s_2} \dot{u}_{s_2} = -m_{s_2} \ddot{u}_g \quad \text{(A.7)} \\
&m_{sd} \ddot{x}_1 - m_{sd} x_1 \alpha^2 \left(\dot{u}_{s_1} - \dot{u}_g \right)^2 + F_{bsd_1} \left(x_1 \right) + c_{sd} \dot{x}_1 = 0 \\
&m_{sd} \ddot{x}_2 - m_{sd} x_2 \alpha^2 \left(\dot{u}_{s_2} - \dot{u}_{s_1} \right)^2 + F_{bsd_2} \left(x_2 \right) + c_{sd} \dot{x}_2 = 0
\end{aligned}$$

In the above equations, F_{bsd_1}, F_{bsd_2} represents the restoring force from the trilinear springs of the VIRM in the 1st and 2nd story and can be expressed as

$$F_{bsd_i} = \begin{Bmatrix} k_{sd}\left(R_{lbc} - x_0\right) + k_p\left(x_i - R_{lbc}\right),\ x_i < R_{lbc} \\ k_{sd}\left(x_i - x_0\right), R_{lbc} \le x_i < R_{ubc} \\ k_{sd}\left(R_{ubc} - x_0\right) + k_p\left(x_i - R_{ubc}\right), x_i \ge R_{ubc} \end{Bmatrix}, i = 1, 2; \tag{A.8}$$

Equation (A.7) is the equations of motion of the 2VIRM structure. The same approach can be taken to derive the equations of motion of the 1VIRM structure. As the 1VIRM structure does not have a VIRM at the 2nd story, the parameter of the that VIRM will be removed from the kinetic energy, potential energy and the non-conservative forces in Equations (A.3), (A.4) and (A.5).